Materials and Design 198 (2021) 109315

Contents lists available at ScienceDirect

Materials and Design

journal homepage: www.elsevier.com/locate/matdes

Enhanced precipitation strengthening of multi-principal element alloys by κ- and B2-phases

Fabian Kies [a,*], Xiaoxiang Wu [b,c], Bengt Hallstedt [d], Zhiming Li [e,c], Christian Haase [a]

[a] Steel Institute, RWTH Aachen University, 52072 Aachen, Germany
[b] Shagang School of Iron and Steel, Soochow University, Suzhou 215137, China
[c] Microstructure Physics and Alloy Design, Max-Planck-Institut für Eisenforschung GmbH, 40237 Düsseldorf, Germany
[d] Materials Applications in Mechanical Engineering, RWTH Aachen University, 52062 Aachen, Germany
[e] School of Materials Science and Engineering, Central South University, Changsha 410083, China

GRAPHICAL ABSTRACT

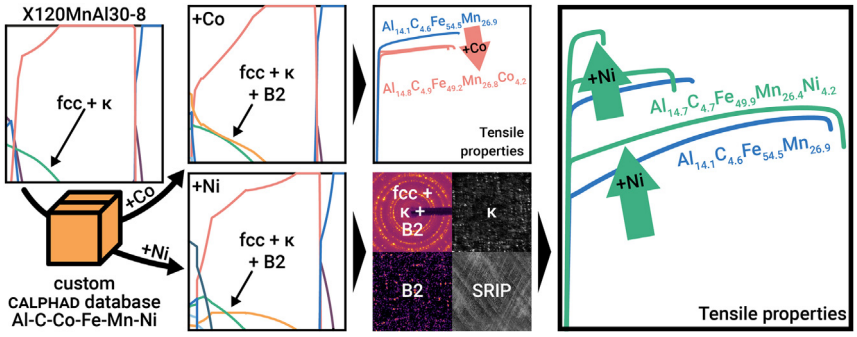

ARTICLE INFO

Article history:
Received 29 September 2020
Received in revised form 4 November 2020
Accepted 8 November 2020
Available online 11 November 2020

Keywords:
High-entropy alloy
Precipitation strengthening
Microband-induced plasticity
Alloy design
Calphad

ABSTRACT

Discoveries of new multi-principal element alloys (MPEAs) with outstanding performance have been challenging due to the large complexity of the compositional space. Many existing highly alloyed steels already incorporate MPEA concepts and detailed research is readily available, which can be utilized for a more efficient design approach. Inspired by this consideration, Ni- and Co-additions to the $Al_{14.6}C_{4.9}Fe_{53.6}Mn_{26.9}$ (at%) high-manganese steel were assessed to introduce B2-precipitates in addition to the κ-carbides to increase strength. Thermodynamic screening in the Al-C-Co-Fe-Mn-Ni system was performed with a custom CALPHAD database and combined with experimental screening to identify novel MPEAs with enhanced mechanical properties. The selected MPEAs were produced by thermo-mechanical processing and the mechanisms active during annealing and deformation were investigated experimentally. The modification with Co did not result in the formation of B2-precipitates and improved mechanical properties. The Ni-added MPEA, $Al_{14.7}C_{4.7}Fe_{49.9}Mn_{26.4}Ni_{4.2}$, revealed significant precipitation and dispersion hardening by nanoscale κ- and B2-phases combined with excellent strain hardening capacity due to slip band refinement-induced plasticity (SRIP). A combination of 1 to 1.2 GPa yield strength (21.3 % increase) with a total elongation of 20 to 10 % was achieved. The chosen methodology was efficient in the design of a novel MPEA with an improved strength-ductility synergy.

1. Introduction

Multi-principal element alloys (MPEAs), also known as high-entropy alloys (HEAs), are a comparatively new class of alloys, which

* Corresponding author.
E-mail addresses: fabian.kies@iehk.rwth-aachen.de (F. Kies), christian.haase@iehk.rwth-aachen.de (C. Haase).

https://doi.org/10.1016/j.matdes.2020.109315

gained much attention in research during the past two decades [1,2]. Instead of relying on one base element, MPEAs are loosely defined as alloys consisting of multiple elements, each with a fraction between 5 and 35 at% [3]. Surprisingly, these alloys often form non-ordered simple crystal structures, such as face-centered cubic (fcc) or body-centered cubic (bcc) [3,4]. The latter is usually explained by high configurational entropy promoting the formation of simple crystal structures at high temperatures, and sluggish diffusion preventing the transformation into more complex phases at low temperatures [5]. As the alloy concept relies on multiple principal elements, MPEAs allow for high degrees of freedom in their chemical and microstructural design. To explore this wide alloy space, several approaches have been employed to screen MPEAs. These were mostly based on CALPHAD-method (CALculation of PHAse Diagrams) [6–8] or *ab initio* [9–12] calculations combined with conventional [6] or high-throughput [11,13,14] manufacturing methods. However, it was also found that the target properties, often mechanical properties, of MPEAs cannot compete with established alloys in most cases [15]. Hence, advancing from single-phase to multi-phase MPEAs has been a scientific target of the research community recently [16].

The present approach aims to bring together the alloying concepts of MPEAs and highly alloyed steels to design novel alloys with enhanced mechanical properties. Lightweight, κ-carbide strengthened high-manganese steels (HMnS) with high Al, Mn and C contents reveal a unique combination of high strength and ductility. This behavior results from strengthening by coherent, nanoscale precipitates and strong strain hardening due to the activation of slip band refinement-induced plasticity (SRIP) [17–22]. The high total elongation of >50 % in these steels allows for further strengthening, since some ductility can be sacrificed for enhanced strength. However, that requires adaption of the chemical composition to promote the formation of additional phases. In both MPEAs [23–25] and austenitic steels [26–32], the incoherent AlNi B2-phase (ordered bcc) was found to act as a suitable phase for efficient precipitation strengthening. Hence, we identified combined κ-carbide and B2-phase strengthening as a promising path to design novel MPEAs with properties that are superior to existing steel concepts.

For computational alloy screening of these types of MPEAs, a custom CALPHAD database was constructed in our previous works [11,33]. The database was compiled from the binary and ternary subsystems of Co-Cr-Fe-Mn-Ni [33] and was extended to Al and C [11]. Even though the database is still in development, it allows for phase prediction and, thus, guided alloy design of Al-C-Co-Cr-Fe-Mn-Ni MPEAs. More specifically, it enables the design of MPEAs based on highly alloyed steels strengthened by κ-carbides and offers new pathways for the efficient computational screening of MPEAs.

Based on our previous investigation [34], the alloy $Al_{14.6}C_{4.9}Fe_{53.6}Mn_{26.9}$ (at%, converted from X120MnAl30–8), which can be strengthened by precipitation of κ-carbides, was used as the reference state and base alloy. The developed CALPHAD database was employed to reveal suitable alloying elements that promote the concurrent formation of κ-carbides and B2-phase in an fcc-based MPEA. Both Ni and Co were identified as suitable candidates that enable the formation of the B2-phase without suppressing κ-carbides. Hence, Ni- and Co-alloyed $Al_{14.6}C_{4.9}Fe_{53.6}Mn_{26.9}$ were produced by ingot casting and post-processed by thermo-mechanical treatment. The precipitation, deformation and fracture behavior were investigated using scanning electron microscopy (SEM), energy-dispersive X-ray spectroscopy (EDS), electron backscatter diffraction (EBSD), electron channeling contrast imaging (ECCI), synchrotron X-ray diffraction (SYXRD), transmission electron microscopy (TEM), and atom probe tomography (APT). The applicability of the proposed methodology for designing MPEAs based on highly alloyed steel concepts and the underlying materials mechanisms are critically discussed.

2. Applied methods

2.1. Phase diagram calculations

The modified custom CALPHAD database [33] was used for thermodynamic screening. Based on the steel composition of $Al_{14.6}C_{4.9}Fe_{53.6}Mn_{26.9}$ (at%) [34,35], additions of Ni and Co were considered, which together with Al promote the formation of the B2-phase. In the thermodynamic calculations, Fe was replaced with up to 8 at% Ni or Co and the results were then compared to calculations without the additions. The ideal B2-phase consists of equal mole fractions of AlNi or CoAl, but experimentally it is usually very far from this composition and may contain Fe and Mn. The design goal was the identification of compositions that are mostly fcc in a relatively wide temperature range above 800 °C with about equal amounts of κ- and B2-phase below 800 °C. Compositions reasonably fulfilling these conditions were found in $Al_{14.6}C_{4.9}Fe_{53.6}Mn_{26.9}$ (referred to as BASE) with 4.2 at% of Ni ($Al_{14.6}C_{4.9}Fe_{49.3}Mn_{26.9}Ni_{4.2}$, referred to as $BASE^{Ni}$) or Co ($Al_{14.6}C_{4.9}Fe_{49.3}Mn_{26.9}Co_{4.2}$, referred to as $BASE^{Co}$).

2.2. Thermodynamic screening

The calculated phase compositions of the alloys are shown in Fig. 1. The BASE alloy is single-phase fcc from about 800 °C up to its solidus temperature at about 1300 °C. Below about 800 °C, the κ-phase is expected to form, but not the B2-phase. Below 500 °C the fcc phase would completely decompose to bcc, β-Mn, κ-phase and $M_{23}C_6$. However, the diffusion rate of all elements except C is too low to enable this complete transformation and the decomposition of the fcc-phase beyond the formation of κ-phase has not yet been reported. All three alloys solidify peritectically, forming up to 40 % bcc before the solidification changes to fcc. Such solidification can lead to non-obvious inhomogeneous distributions of the alloying elements since the partitioning to the bcc and fcc phases is different. According to the calculation, the $BASE^{Ni}$ alloy is single-phase between 1150 and 1300 °C. Below 800 °C, the precipitation of both κ- and B2-phase is expected and below 550 °C the B2-precipitation is increasingly replaced by L12 with an ideal composition of Ni_3Al. In the $BASE^{Co}$ alloy, about equal amounts of κ- and B2-phase are expected to precipitate between 500 and 800 °C. Below 500 °C, the disordered fcc phase is no longer stable, but its decomposition is expected to be too slow to be observed. Above about 950 °C, the alloy is expected to be single-phase fcc up to its solidus just below 1300 °C. The annealing temperatures were based on the expected precipitation of B2-, B2/κ - or B2/κ/ $L1_2$-phases in fcc, as indicated in Fig. 1.

2.3. Material and processing

Both $BASE^{Ni}$ and $BASE^{Co}$ alloys were prepared by vacuum induction melting with input materials containing >99.8 % purity. Water jet cutting was used to produce ~12 mm sheets, which were then subjected to the processing route schematically shown in Fig. 2. Thus, they were hot rolled at 1150 °C to 4 mm thickness and subsequently homogenized for 5 h (state HM). After air cooling, cold rolling was performed with a reduction of 50 % down to 2 mm (state CR). Further heat treatments were performed according to the thermodynamic calculations. First, the sheet was recrystallized in the single-phase fcc region at 1200 °C for 3 min followed by water quenching to obtain a fully austenitic microstructure (state RX). Aging was then performed at the temperatures indicated in Fig. 1 with aging times ranging from 15 min to 16 h followed by water quenching (state aged), and will be referred to as *Alloy ([temperature]/[time])*. The chemical compositions obtained by wet-chemical analysis after processing of the investigated alloys are given in Table 1.

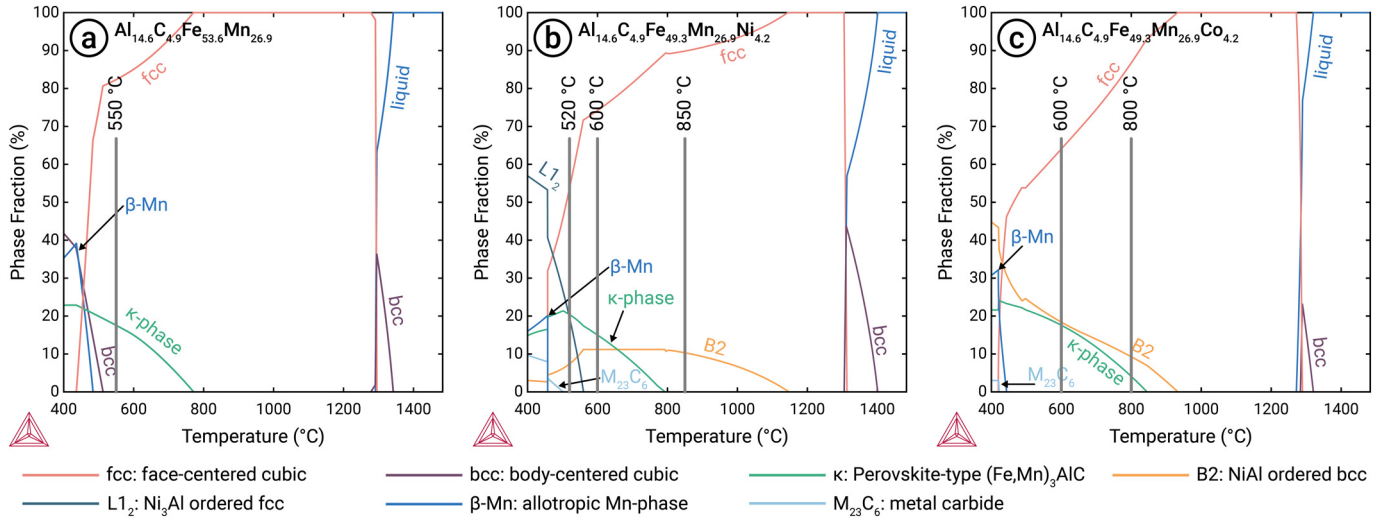

Fig. 1. Equilibrium phase fractions over temperature diagram for (a) BASE [34], (b) BASE^{Ni} and (c) BASE^{Co} calculated with the CALPHAD-method using the custom database. In BASE, the highest fraction of the κ-phase in the fcc-matrix was obtained by annealing at 550 °C [34]. The annealing temperatures for BASE^{Ni} and BASE^{Co} are also shown and were based on the expected precipitation of B2-, B2/κ- or B2/κ/$L1_2$-phases in the fcc-matrix.

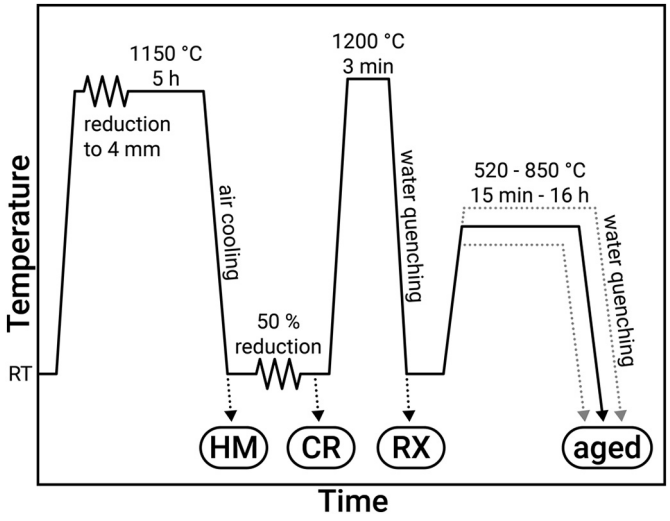

Fig. 2. Thermo-mechanical processing route applied in the present study. Samples were investigated in the homogenized (HM), cold rolled (CR), recrystallized (RX) and aged states.

2.4. Microstructure characterization techniques

Microstructure specimens with dimensions of 12×10×2 mm^3 (rolling direction (RD) × transverse direction (TD) × normal direction (ND)) were cut by electrical discharge machining. Specimens for analysis of the deformed microstructure were taken close to the fracture surface of the tensile samples in the RD×ND plane. For SEM and EBSD analysis, the samples were first ground with up to 1200 SiC grit paper followed by mechanical polishing using 6 and 1 μm diamond suspensions. Finally, they were electrolytically polished at 20 (BASE^{Ni}) or 24 (BASE^{Co}) for 15 s in Struers A2 electrolyte. For ECCI and TEM analysis, samples were ground with 400 to 2500 SiC grit paper and mechanically polished using 3 and 1 μm diamond suspensions. Subsequently, the samples were fine-polished in an oxide polishing suspension (OPS) containing 50 nm silica particles for 30 min. The sample surfaces were cleaned with soap and water to remove the residual nano-silica particles.

Various SEM methods including secondary electron (SE) imaging, EBSD and EDS were performed on a Zeiss Sigma field emission gun (FEG) SEM with EBSD and EDS detectors by Oxford. For EBSD analysis, a voltage of 20 kV was chosen with a working distance between 16 and 18 mm and a step size of 1 μm. Analysis and noise reduction of the EBSD data was carried out with the MATLAB® based MTEX toolbox [36,37]. The grain size was determined by merging grains along annealing twins and calculating the mean equivalent diameter of the grain area as a circle. SE micrographs and EDS were recorded at a voltage of 15 kV with a working distance between 8 and 9 mm for the microstructure and between 10 and 15 mm for the fracture surfaces. ECCI was conducted in a Zeiss-Merlin instrument using a voltage of 30 kV and a current of 2 to 4 nA.

SYXRD was performed on the P02.1 powder diffraction beamline at DESY, Hamburg, with a wavelength of 0.20682 Å for recording diffraction patterns on a PerkinElmer XRD1621 fast area detector. The data were integrated into 1D diffractograms using Fit2D [38,39]. Complete rings were analyzed within a range of 2Θ from 2.85° to 11.35°. Subsequent analysis of the phase fractions was performed with a Rietveld analysis using the open-source software Material Analysis Using Diffraction (MAUD) [40].

TEM analysis was conducted using an image-corrected FEI Titan Themis 80–300 operated at 300 kV. A site-specific focused ion beam (FIB) lift-out procedure was adapted using a dual-beam FEI Helios Nanolab 600i FIB instrument. Selected area electron diffraction (SAED) patterns were simulated using the open-source software Phase Transformation Crystallography Lab (PTCLab) [41].

A LEAP 5000 XR from Cameca Instruments Inc. operated in voltage-pulsing mode was used for atom probe tomography (APT). A pulse repetition rate of 200 kHz was used and the specimen was kept at a base temperature of 60 K. The detection rate was kept at a frequency of 0.5 ions per 100 pulses on average and a pulse fraction of 15 %. The APT data were analyzed with the IVAS software 3.8.4.

Table 1
Chemical composition of the investigated alloys. The composition of BASE was taken from Ref. [34]. Measurements were taken in wt% and converted to at%.

	Sample	Fe	C	Mn	Al	Ni	Co	S*	P*	N*
(wt%)	BASE	bal.	1.11	29.8	7.65	–	–	170	–	83
	BASE^{Ni}	bal.	1.15	29.4	8.02	5.00	–	116	75	25
	BASE^{Co}	bal.	1.19	29.9	8.10	–	5.07	129	90	27
(at%)	BASE	54.50	4.58	26.87	14.05	–	–			
	BASE^{Ni}	49.93	4.73	26.44	14.69	4.21	–			
	BASE^{Co}	49.22	4.89	26.84	14.81	–	4.24			

* in ppm.

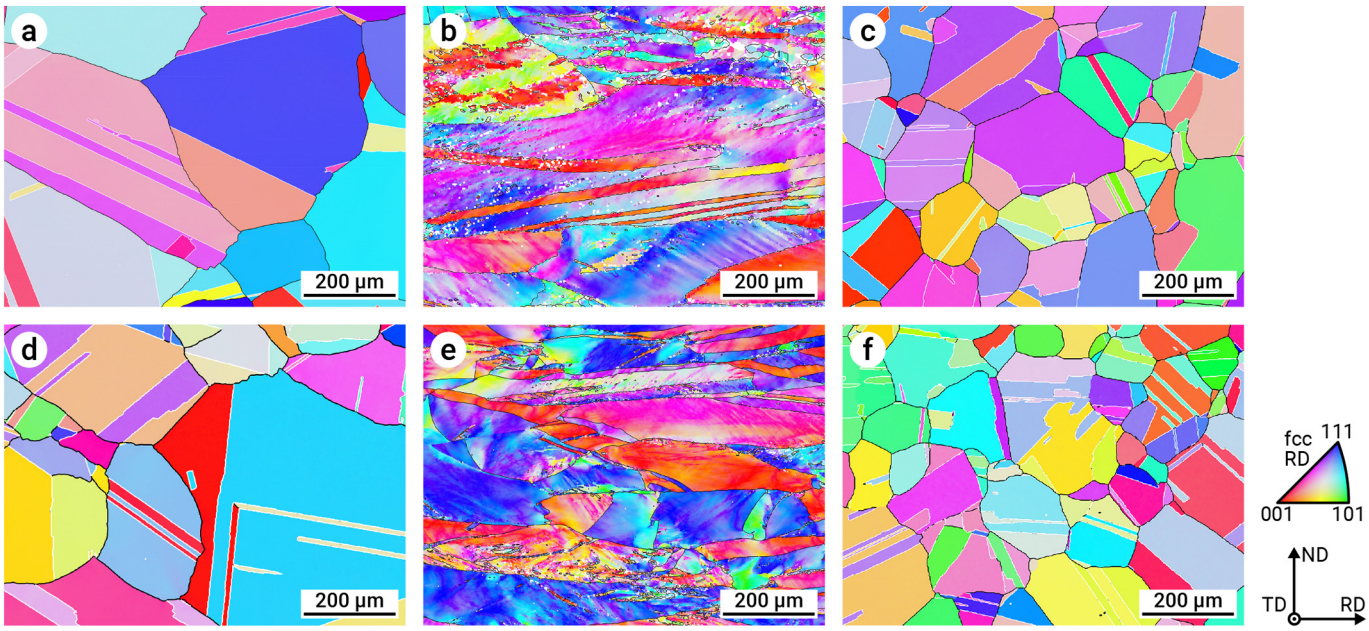

Fig. 3. EBSD maps colored with respect to the inverse pole-figure (IPF) with RD as reference axis for (a–c) BASE^{Ni} and (d–f) BASE^{Co}. The maps are shown for the (a, d) HM, (b, e) CR and (c, f) RX states. Black and white lines denote general high-angle (>10°) and Σ3 (60° around ⟨111⟩) grain boundaries, respectively. The mean grain size excluding twin boundaries was calculated as (a) 212 µm, (c) 155 µm, (d) 183 µm and (f) 119 µm.

2.5. Mechanical characterization techniques

The Vickers hardness was determined on a Wolpert Instron TESTOR 930 with a force of 294.2 N (HV30) on the polished RD-ND plane of the microstructure samples. The mean value from three measurements was taken for each sample. Dog bone-shaped specimens with a cross-section of 2×2 mm^2 (TD×ND) and a gauge length of 13 mm (RD) were prepared from the sheets via electrical discharge machining. Quasi-static uniaxial tensile tests were then performed on a Z4204 Zwick/Roell device at room temperature with a strain rate of 2.5×10^{-4} s^{-1}.

3. Results

3.1. Initial microstructure

In Fig. 3, the microstructures from EBSD analyses are shown in HM, CR and RX condition for the BASE^{Ni} and BASE^{Co} alloys. A single-phase fcc microstructure was measured in each state. After HM (1150 °C/5 h) and RX (1200 °C/3 min) annealing, a fully recrystallized microstructure with annealing twins was obtained. Compared to the HM state, the grain size in RX was reduced from 212 to 155 µm in BASE^{Ni} and from 183 to 119 µm in BASE^{Co}.

3.2. Mechanical properties

The hardness evolution during the annealing treatments (see Fig. 1) is shown in Fig. 4. Annealing in the fcc+B2 region barely influenced the hardness in either investigated alloy. In the BASE^{Ni} alloy (Fig. 4a) annealed in the fcc+B2+κ region, the hardness increased moderately up to 4 h, after which it increased more strongly as indicated in a slope transition. In contrast, specimens annealed in the fcc+B2+κ+L1$_2$ region were characterized by an overall lower hardness without a slope transition. In the BASE^{Co} alloy (Fig. 4b) annealed in the fcc+B2+κ

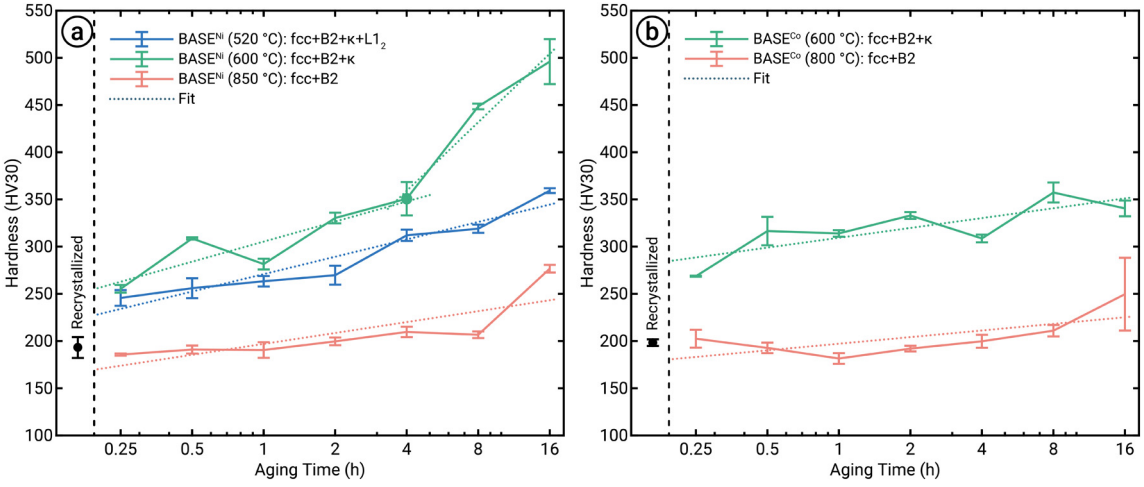

Fig. 4. Development of the mean Vickers hardness during annealing at different temperatures for the (a) BASE^{Ni} and (b) BASE^{Co} alloys. The respective annealing temperature resulted in varying precipitation states (see Fig. 1). Annealing for B2-phase in fcc (at 850 °C in BASE^{Ni} and 800 °C in BASE^{Co}) did hardly affect the hardness evolution.

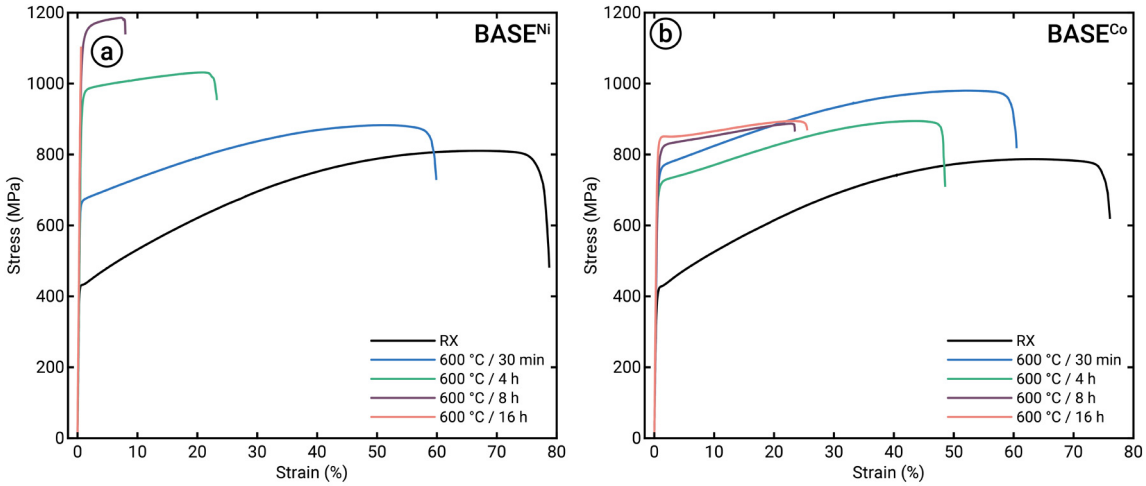

BASE^{Ni}	RX	600 °C 30 min	600 °C 4 h	600 °C 8 h	600 °C 16 h
$R_{p0.2}$ (MPa)	428	659	934	1067	–
R_m (MPa)	811	883	1032	1186	–
A_g (%)	66.3	50.4	20.3	6.7	–

BASE^{Co}	RX	600 °C 30 min	600 °C 4 h	600 °C 8 h	600 °C 16 h
$R_{p0.2}$ (MPa)	392	721	678	738	817
R_m (MPa)	787	980	894	887	895
A_g (%)	62.0	51.5	43.6	22.2	23.1

Fig. 5. Engineering stress-strain curves and characteristic values (yield strength $R_{p0.2}$, ultimate tensile strength R_m, uniform elongation A_g) for the (a) BASE^{Ni} and (b) BASE^{Co} alloys in the recrystallized (RX) and 600 °C annealed states.

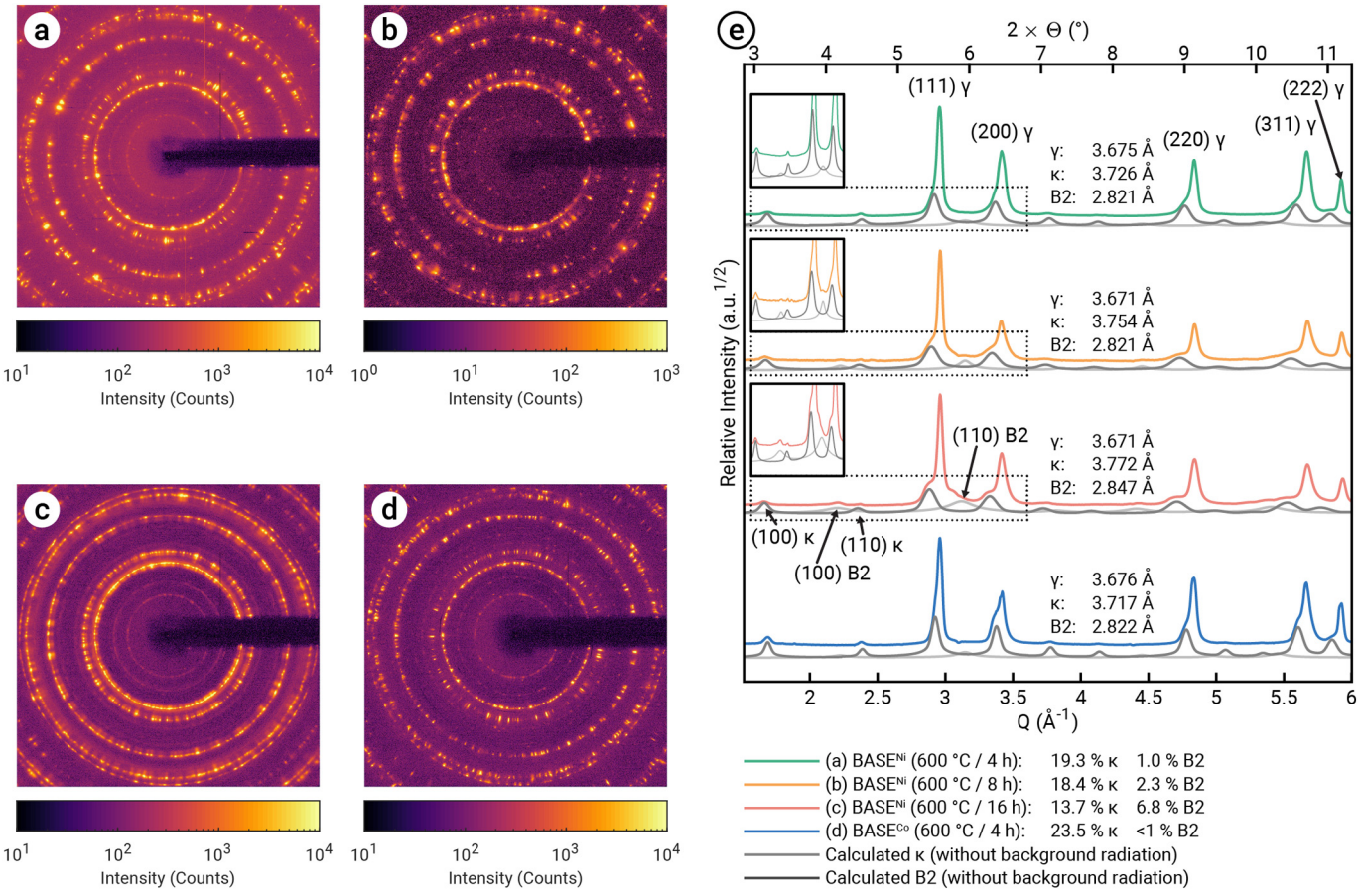

Fig. 6. SYXRD (a to d) 2D patterns displayed with logarithmic intensity, which were integrated into (e) 1D diffractograms using Fit2D [38,39]. The phase fractions of the κ- and B2-phases were determined by a Rietvelt analysis using MAUD [40], where the superlattice reflection for the κ- and B2-phases were carefully fitted for the determination of the lattice constants. The ideal, calculated 1D diffractograms without background radiation are overlaid in each measurement to show the (hkl) peak locations. In the BASE^{Ni} samples, the fraction of κ-phase decreased from 4 to 16 h, while the fraction of B2-phase increased. In the BASE^{Co} (600 °C/4 h) alloy, 23.5 % κ-phase and only trace amounts of B2-phase were calculated.

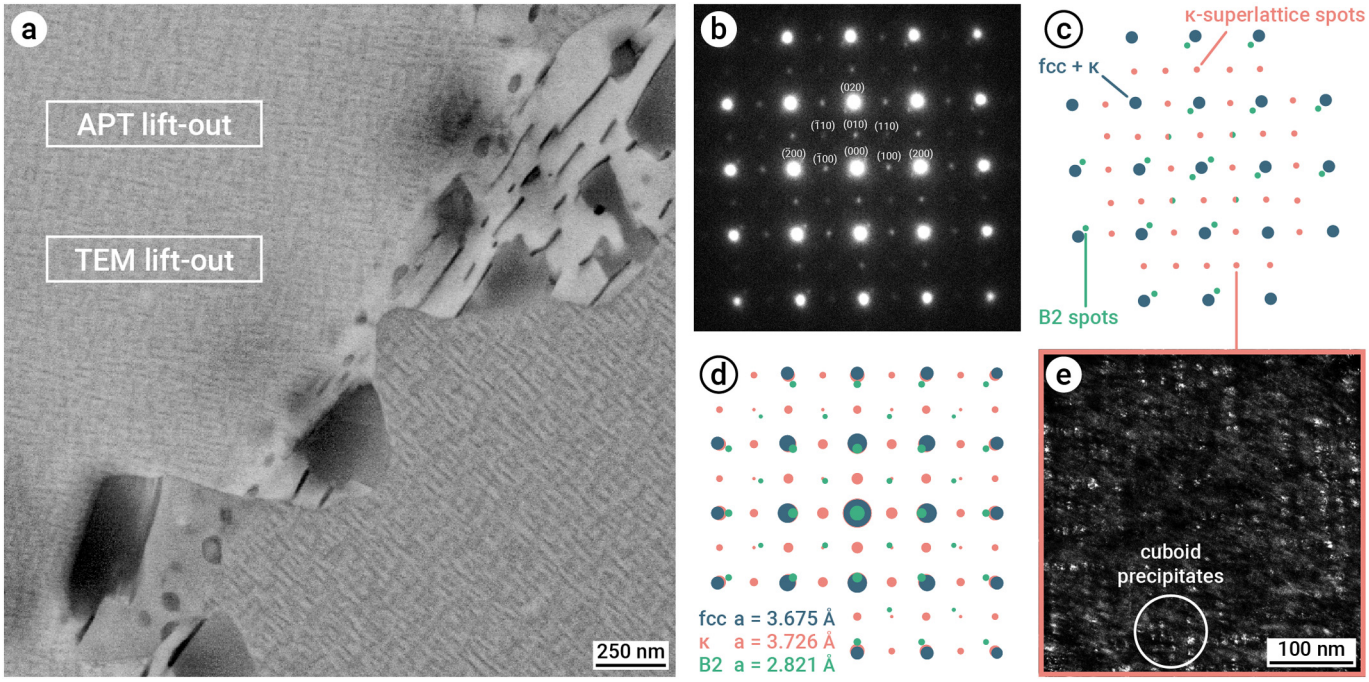

Fig. 7. (a) ECCI micrograph of the BASE^{Ni} (600 °C/4 h) alloy, showing grain boundary precipitates, basketweave-type precipitates in the matrix and the area for the TEM (Figs. 8 and 13) and APT (Fig. 9) lift-out. The matrix precipitates were further characterized by TEM with (b) ⟨001⟩ SAED pattern and the corresponding (c) indexed fcc, Perovskite- (κ) and B2-phase spots. (d) The SAED pattern was simulated using these phases, the lattice parameter in Fig. 6 and a 45° rotation of the B2-phase around the ϕ_1-axis. (e) Dark field (DF) image for the κ-phase using the respective superlattice diffraction spots showing a cuboidal precipitate morphology.

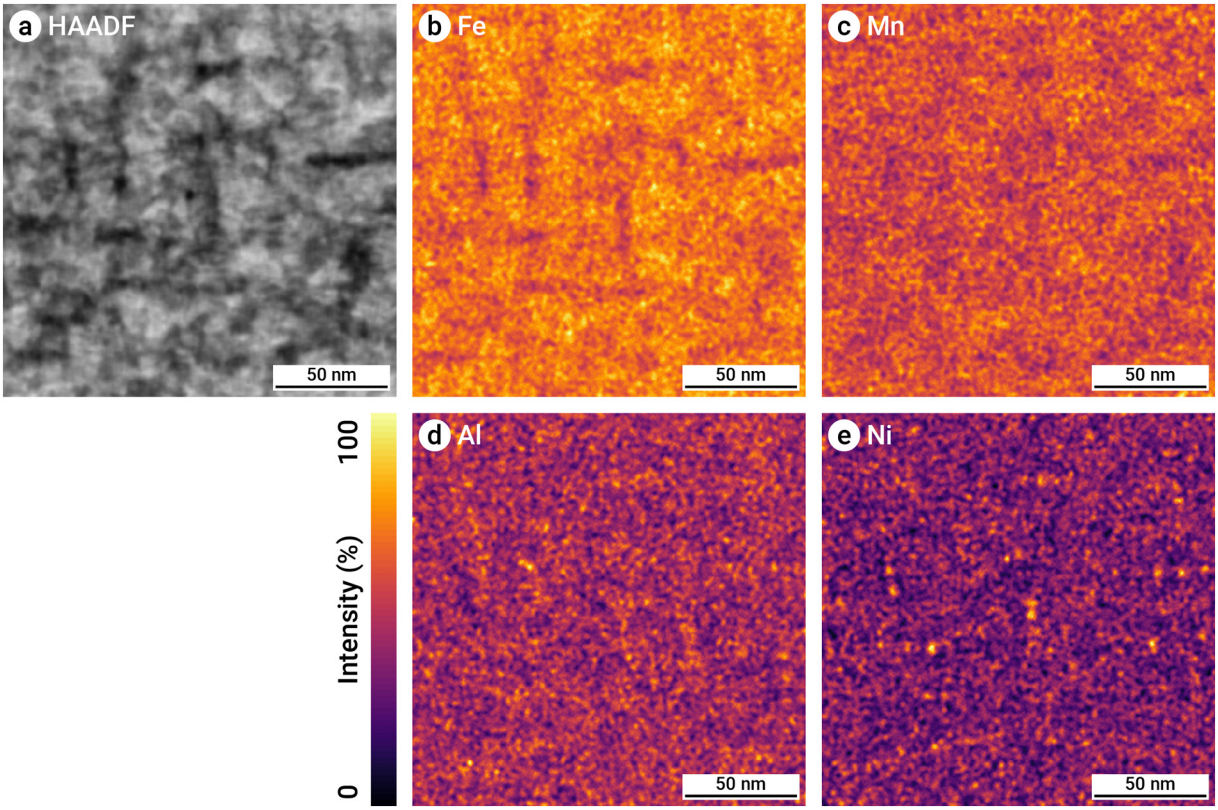

Fig. 8. (a) High-angle annular dark-field (HAADF) image and (b to e) corresponding STEM EDS maps from the lift-out indicated in Fig. 7a. The basketweave precipitate structure was depleted in Fe with high-intensity spots of Ni.

region, only a minor increase in hardness was observed with increasing time.

Based on the highest hardness after annealing at 600 °C (see Fig. 4), the mechanical properties of these specimens were investigated in more detail by tensile testing (Fig. 5). In the BASE^{Ni} alloy (Fig. 5a), annealing up to 8 h resulted in higher yield strength ($R_{p0.2}$, 428 to 1067 MPa) and ultimate tensile strength (R_m, 811 to 1186 MPa), while the uniform elongation (A_g) decreased from 66.3 to 6.7 %. After annealing for 16 h, brittle failure occurred within the elastic region. Annealing of the BASE^{Co} alloy (Fig. 5b) for 30 min resulted in an increase of $R_{p0.2}$ from 392 to 721 MPa and R_m from 787 to 980 MPa. With increased annealing time, A_g decreased from 43.6 to 23.1 %, while R_m remained constant at ~892 MPa.

3.3. Precipitate analysis

The results of the SYXRD phase analysis are shown in Fig. 6. Based on the slope transition in the hardness curves (see Fig. 4a), the BASE^{Ni} samples annealed at 600 °C for 4 to 16 h were investigated. The 2D patterns did not manifest in continuous rings due to the coarse grain size (see Fig. 3). κ- and B2-phase superlattice reflections were clearly detected and both phases were present in the samples. With increasing annealing time, the fractions of κ-phase decreased from 19.3 to 13.7 vol%, while the fraction of B2-phase increased from 1.0 to 6.8 vol%. Furthermore, the lattice parameters for the κ- and B2-phases increased with extended annealing from 3.726 to 3.772 Å and from 2.821 to 2.847 Å, respectively, while the fcc lattice parameter remained unaffected at ~3.671 Å. For the BASE^{Co} alloy, the state annealed at 600 °C for 4 h was analyzed. A fraction of 23.5 vol% κ-phase was detected with trace amounts of B2-phase. Furthermore, the narrower peak corresponding to the κ-phase indicated coarser precipitates in BASE^{Co} compared to the BASE^{Ni} alloys.

As a preliminary database was used, the thermodynamic calculations can lead to imprecise results. This was the case with the BASE^{Co} alloy, where the formation of the B2-phase and its strengthening effect was not observed. The accuracy of the custom database for MPEAs are part of a separate investigation. Therefore, more detailed characterizations of the microstructural development were limited to the BASE^{Ni} alloy annealed at 600 °C. Specifically, a second hardening stage appeared after annealing for 4 (Fig. 4a).

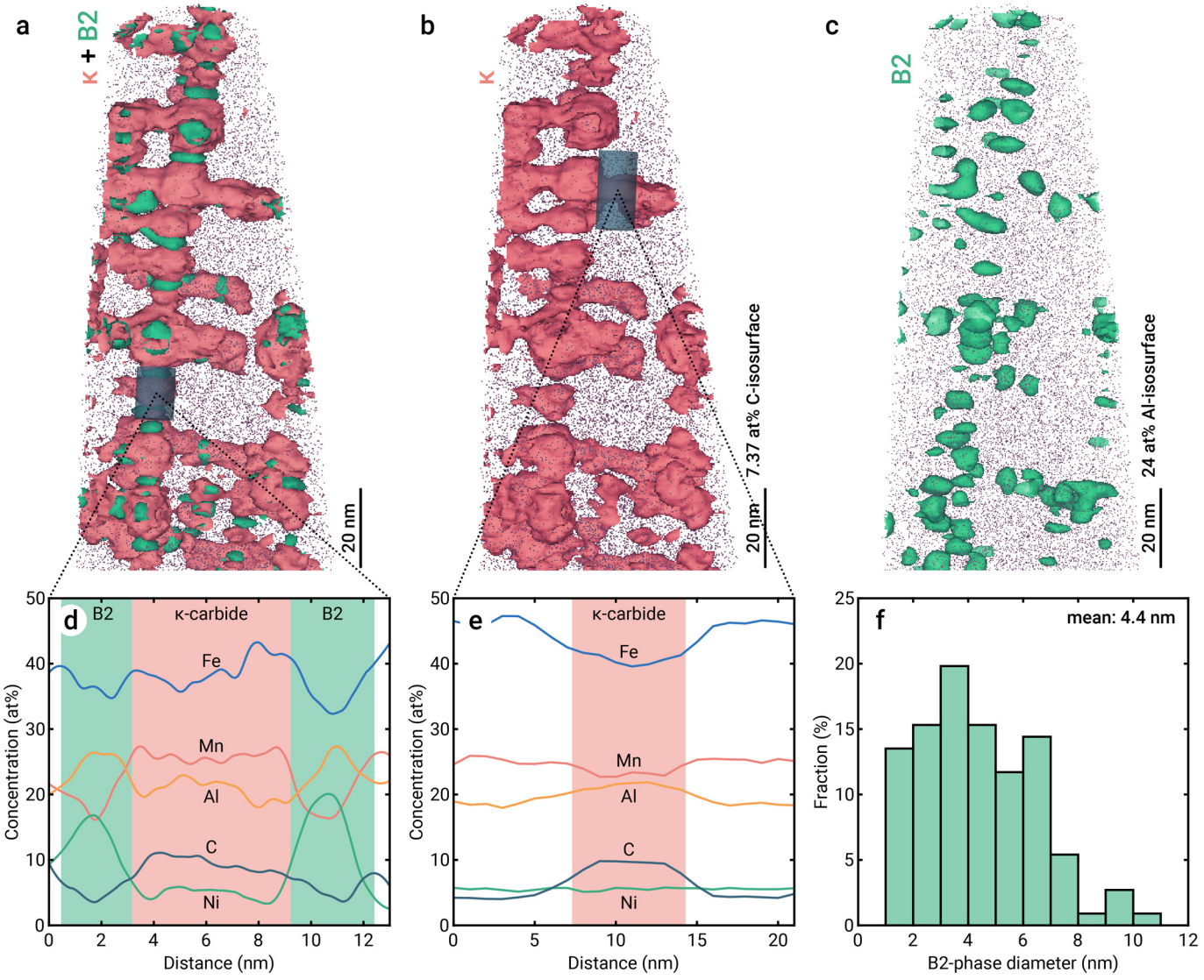

Fig. 9. APT analysis of the BASE^{Ni} (600 °C/4 h) alloy showing (a) both κ-carbides and the B2-phase, (b) only κ-carbides (7.37 at% C-isosurface) and (c) only the B2-phase (24 at% Al-isosurface). A 3D-representation of the results can be found in the Supplementary Data. (d, e) 1D concentration profiles showing the chemical composition of κ-carbides and the B2-phase. (f) Histogram and mean diameter of the detected B2-phase. The diameter d was calculated by assuming that the area of each isosurface A covers a sphere, where $A = \pi d^2$.

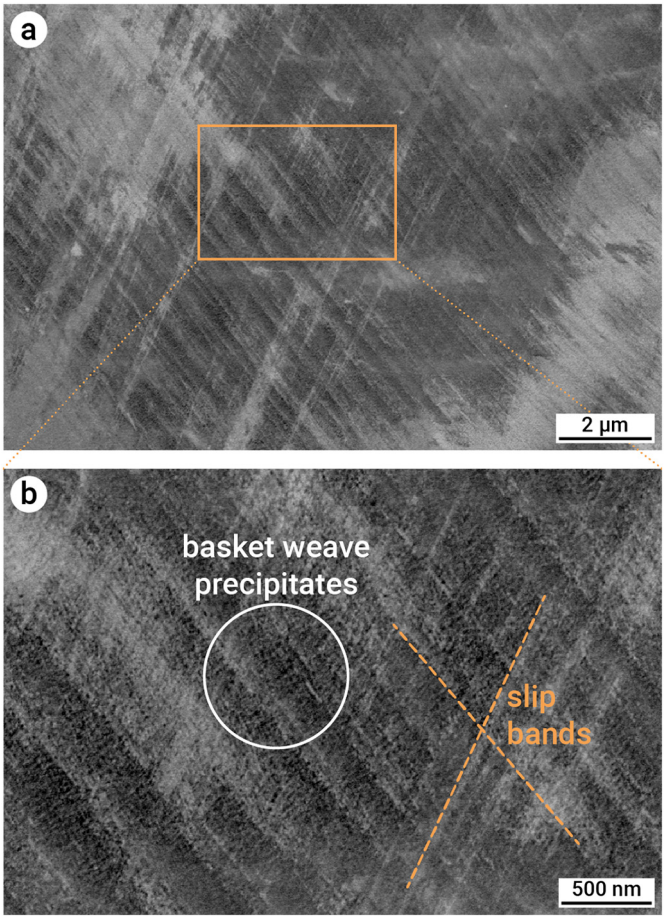

Fig. 10. ECCI taken from a sample region close to the fracture surface of the BASE^{Ni} (600 °C/4 h) tensile sample. The formation of slip bands on two non-coplanar slip planes was observed, confirming the activation of the SRIP effect. The morphology of slip bands was not influenced by the precipitates.

Precipitate formation within the fcc matrix of the BASE^{Ni} (600 °C/4 h) alloy was analyzed by ECCI and TEM (Fig. 7). The precipitates manifested in a basketweave type structure (Fig. 7a). Further analysis of the corresponding SAED patterns (Fig. 7b and c) revealed fcc spots and superlattice reflections for the $E2_1$ κ-phase as well as satellite spots around the fcc peaks. The simulation of the pattern (Fig. 7d) revealed the B2-phase rotated by 45° around the ϕ_1-axis as the phase being responsible for the satellite spots according to the lattice parameters of the constituting phases. It should be mentioned that the detected superlattice reflections of ⟨110⟩ cannot be definitively assigned to the κ- or B2-phase because of overlapping patterns and generally low intensities. The dark field (DF) image (Fig. 7e) showed a cuboidal morphology of the κ-phase with a precipitate size of ~10 nm.

The matrix precipitates were further analyzed by STEM EDS (Fig. 8), where the basketweave precipitate structure was visible as dark areas in Fig. 8a. The basketweaves had a width of ~10 nm and were depleted in Fe (Fig. 8b). Additionally, high-intensity spots of Ni (Fig. 8e) were observed within the precipitate structure.

The APT analysis in the BASE^{Ni} (600 °C/4 h) alloy is shown in Fig. 9. The B2-precipitates were found to be adjacent to the κ-carbide (Fig. 9a) and were characterized by a small size of about 4.4 nm (Fig. 9f). In contrast to the $(Fe,Mn)_3AlC_x$ κ-carbides, the B2-phase was enriched in Ni and Al and depleted in C, Mn and Fe (Fig. 9d and e).

3.4. Deformation and fracture behavior

The microstructure close to the fracture surface of the BASE^{Ni} (600 °C/4 h) sample is shown in Fig. 10. In the deformed microstructure, two exclusive non-coplanar slip planes were detected to which the dislocation movement was confined. The basketweave-shaped precipitates can be found between and inside the slip bands.

The tensile fracture surfaces for the BASE^{Ni} alloys annealed at 600 °C are shown in Fig. 11. Increasing annealing times first led to fully ductile (30 min, Fig. 11a), small amounts of intergranular (4 h, Fig. 11b), predominantly intergranular (8 h, Fig. 11c) and finally intragranular fracture (16 h, Fig. 11d).

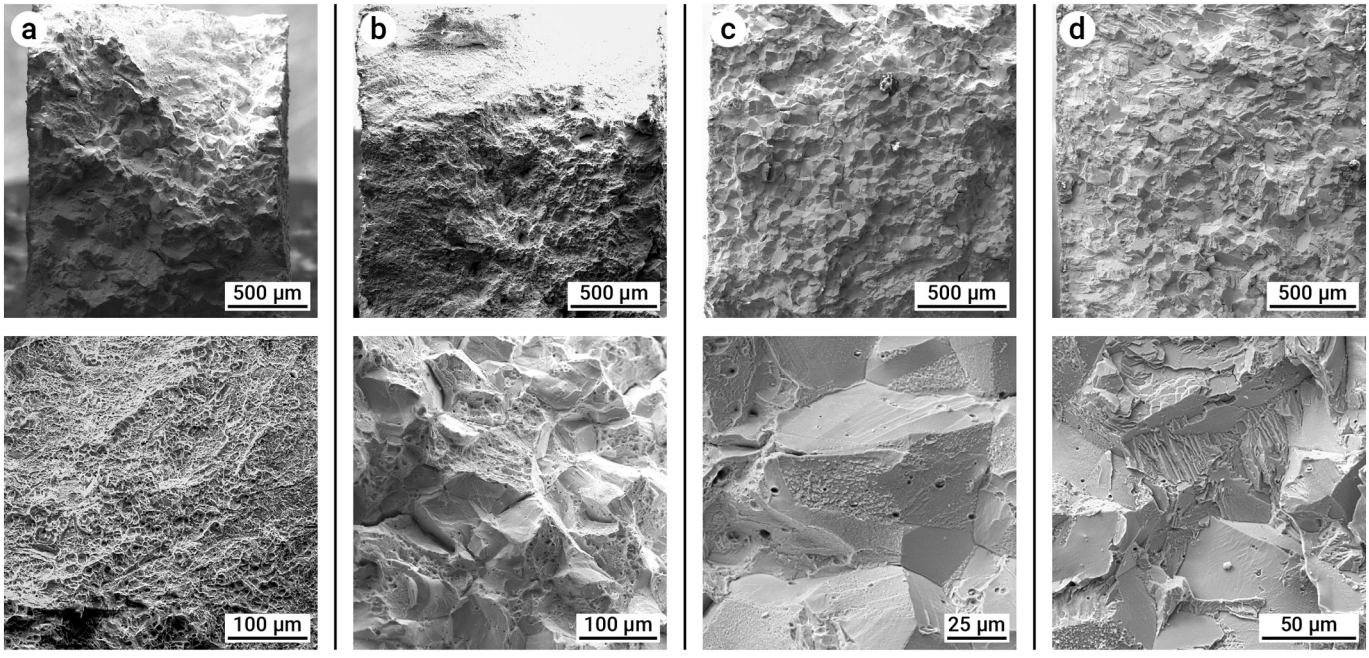

Fig. 11. SEM micrographs of fracture surfaces after tensile testing of the BASE^{Ni} alloys annealed at (a) 600 °C/30 min, (b) 600 °C/4 h, (c) 600 °C/8 h and (d) 600 °C/16 h. With increased aging time, the fully ductile behavior transformed to inter- (8 h) and intragranular (16 h) fracture.

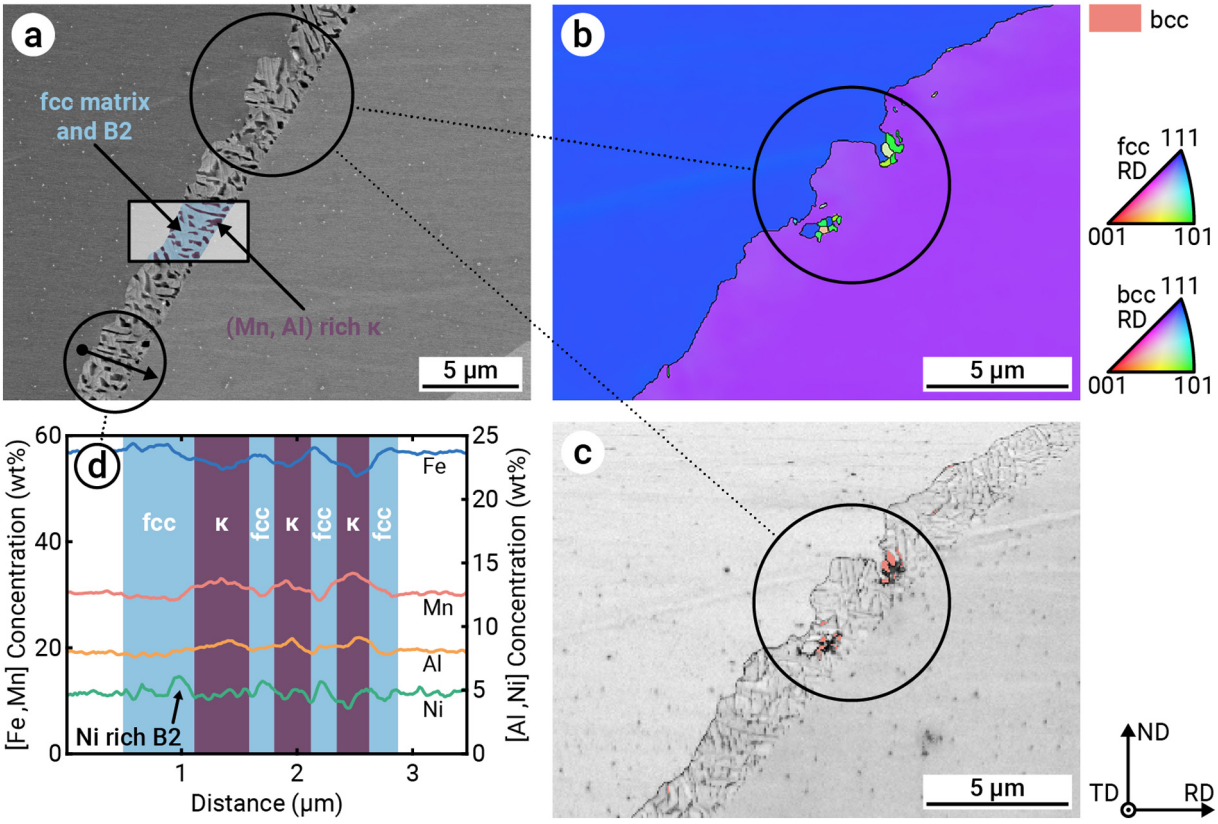

Fig. 12. Microstructure analysis of phases formed at the grain boundaries of the BASE^{Ni} (600 °C/8 h) alloy. The thickness of the phase varied in different grain boundaries around 4 μm and a representative location was chosen. (a) BSE micrograph with corresponding (b) IPF overlaid EBSD maps and (c) IQ with phase. An (d) EDS line scan was performed at the grain boundary, showing increased Mn and Al contents in the purple-marked phase and Ni-rich B2-phase. (For interpretation of the references to colour in this figure legend, the reader is referred to the web version of this article.)

Even though a thin grain boundary phase was detected in the BASE^{Ni} (600 °C/4 h) alloy (Fig. 7a), intergranular fracture was most prominent in the BASE^{Ni} (600 °C/8 h) alloy (Fig. 11c). One representative grain boundary phase is shown in Fig. 12 and was investigated in more detail by EBSD and EDS. Two phases, a bright and a dark one, were observed in the BSE micrograph (Fig. 12a) and were found to be fcc, as shown in the EBSD map in Fig. 12b. Additionally, a small fraction of bcc phase was detected (Fig. 12c). The EDS line scan inside the two-phase structure (Fig. 12d) revealed the dark phase to be enriched in Mn and Al, while the bright phase had a similar composition to the matrix. Spots inside the phase showed high intensities of Ni, which may be caused by an AlNi B2-phase. While the grain boundary phase coarsened from 4 to 16 h annealing, the composition was similar between the different states.

4. Discussion

A custom CALPHAD database was used for thermodynamics-based screening of Al-C-Fe-Mn-Ni/Co MPEAs, aiming at an fcc-based MPEA with κ- and B2-strengthening. 4.2 at% Ni or Co were added to the $Al_{14.6}C_{4.9}Fe_{53.6}Mn_{26.9}$ (at%) BASE alloy to promote the formation of B2-precipitates in addition to κ-carbides. The BASE^{Co} MPEA did neither reveal significant precipitation of the B2-phase nor strength enhancements compared to the BASE alloy. In contrast, the BASE^{Ni} MPEA showed strongly increased strength as a result of B2-phase formation. For the latter alloy, the strength increase was most pronounced following annealing at 600 °C (see Fig. 4a and Fig. 5a) due to the combined formation of the B2- and κ-phase. The strength evolution during annealing can be subdivided into two regimes that are predominantly caused by either the formation of κ-carbides (<4 h) or the B2-phase (≥4 h).

4.1. Formation of κ-carbides in the BASE^{Ni} alloy

In the first strengthening regime (600 °C/<4 h), only small amounts (<1.0 vol%) of B2-phase and predominantly κ-carbides were formed (see Fig. 6). The SYXRD, TEM and APT analyses (Figs. 6, 7 and 9) confirmed the presence of the coherent $(Fe,Mn)_3AlC_x$ κ-carbides with an $E2_1$ Preovskite structure [42] by their superlattice reflections. After 4 h annealing, coherent and cubic κ-precipitates with a size of ~10 nm and a fraction of 19.3 vol% were formed within the fcc matrix (Fig. 7e). The amount is similar to the fractions predicted by CALPHAD (Fig. 1b) and also coincides with the amount of κ-phase detected in similarly annealed BASE samples [35]. Additionally, the cubic κ-phase was arranged in a basketweave pattern resulting from spinodal decomposition, which agrees with the formation process in the BASE alloy [34,43] and other κ-carbide strengthened HMnS [17,44–49]. Extended annealing resulted in a lattice parameter increase from 3.726 to 3.772 Å due to the enrichment of C in the κ-phase [50,51]. Consequently, the modification performed in the BASE alloy by 5 wt% Ni addition had a negligible influence on the precipitation of κ-carbides until 4 annealing at 600 °C.

After annealing at 600 °C between 4 and 16 h, the fraction of κ-carbides decreased from 19.3 to 13.7 vol%. This effect coincided with the formation of the Al- and Ni-rich B2-phase after the incubation period of 4 h (see Sec. 4.2). At shorter annealing times, the added Ni to the BASE alloy had a negligible influence on the formation behavior and volume fraction of the κ -carbides. However, the beginning of the B2-phase formation at 4 h did not only promote the depletion of Al in the matrix, but also the partial dissolution of Al from adjacent κ-carbides, which lowered their thermodynamic stability [17,42,52]. According to the

CALPHAD calculation, 14.1 % κ- and 11.2 % B2-phase are predicted at 600 °C. The result matches the fraction of the κ -phase after 16 h (see Fig. 6c) well. To reveal the phase formation before the formation of the B2-phase, an additional calculation was made that excluded the B2-phase from the equilibrium, i.e. only fcc and κ-phase were allowed to form. Accordingly, the calculated amount of κ-phase was 18.4 %, which corresponds well with the amount of κ-carbides found after 4 h annealing (see Fig. 6a). Hence, the formation of κ-carbides was completed before the nucleation of the B2-phase was initiated. The performed CALPHAD calculations can be found in the Supplementary Data.

4.2. Formation of B2-phase in the BASE^{Ni} alloy

Annealing at 600 °C for 4 h resulted in the formation of the B2-phase besides κ-carbides. With the measured and simulated SAED patterns of the matrix (see Fig. 7b–d), the formation of the B2-phase with a rotation of 45° around the ϕ_1-axis of the fcc matrix was revealed. This confirms the orientation relationship of $\left(1\bar{1}1\right)_{B2} \parallel (200)_{fcc}$ and $[001]_{B2} \parallel [001]_{fcc}$ for B2-phase containing fcc MPEAs [53]. This B2-phase is Al- and Ni-rich and forms within the basketweave precipitate structure, which can be seen in the APT measurement (Fig. 9) and the analysis of the EDS STEM data in Fig. 13. The precipitate structure contains the κ-carbides formed at shorter annealing times by spinodal decomposition (see Sec. 4.1, Fig. 9b, Fig. 13b and c). Since the B2-phase was detected adjacent to the κ-carbides (see Fig. 9a, Fig. 13f), nucleation occurred preferably at coherent κ/matrix-interfaces. Furthermore, both the size distribution of the B2-phase from APT (see Fig. 9f) and the high-intensity spots of the B2-phase (see Fig. 13e) revealed a spherical shape with a diameter of <5 nm, roughly half that of the κ-carbides (see Fig. 7). The observed spherical shape conforms with previous studies on B2-phase containing austenitic steels [26,54].

In contrast to the κ-phase, the incoherent B2-phase [26,30,54] formed by nucleation and growth mechanisms, as substantiated by the incubation period of about 4 h. As stated above, large amounts of nucleation sites were available in the form of coherent phase boundaries between the fcc-matrix and the κ-phase. Consequently, numerous finely dispersed and nano-sized B2-precipitates form inside the fcc matrix. It should be noted that the small B2-phase size also makes detection by SYXRD challenging, as considerable peak broadening can occur within the detected size range of <10 nm [55]. Therefore, the (100) and (110) B2-phase peaks appear very shallow in the diffraction patterns (see Fig. 6), which leads to faint superlattice reflections and considerable peak overlapping. As the broadening effect does not disappear after 8 and 16 h, nano-sized B2-precipitates were retained during extensive annealing. Furthermore, negligible amounts of B2-phase were found at the grain boundaries (Fig. 12) and the detected B2-phase fraction is predominantly located in the matrix. Extended annealing times of 4, 8 and 16 h resulted in an increased volume fraction of 1.0, 2.3 and 6.8 vol% B2-phase, respectively (see Fig. 6).

4.3. Tensile test behavior of the new BASE^{Ni} MPEA

A comparison of the tensile properties of the alloys BASE^{Ni} with BASE is given in Fig. 14. The progression of the strain hardening curves in the BASE^{Ni} RX and (600 °C/30 min) annealed states (Fig. 14b) showed the formation of another hardening stage at the beginning of plastic deformation, where the strain hardening rate increased again. This is

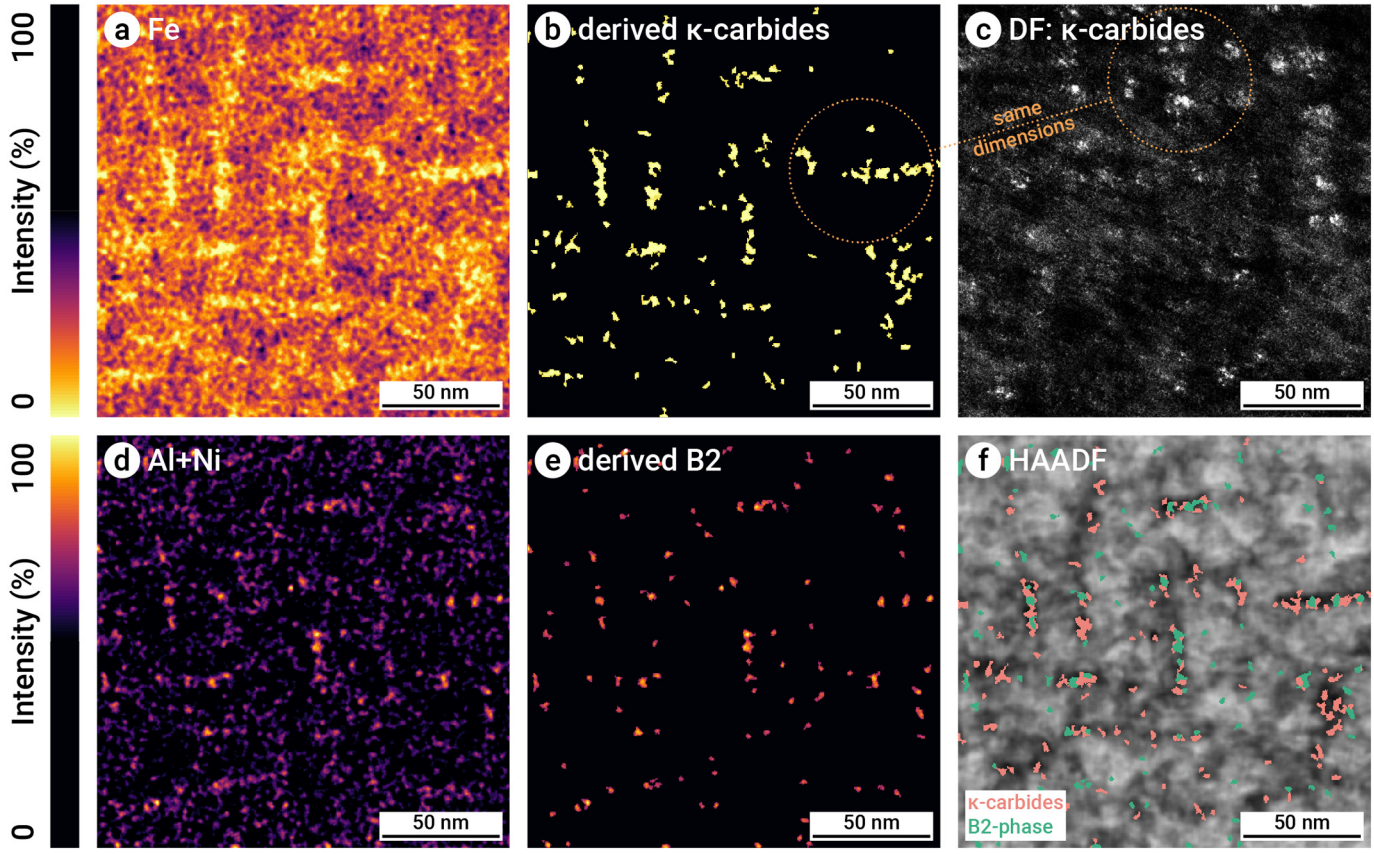

Fig. 13. Precipitate analysis in the BASE^{Ni} alloy (600 °C/4 h) using the STEM EDS data from Fig. 8 with modified intensity scaling. The $(Fe,Mn)_3AlC_x$ κ-carbides contain fewer Fe than the matrix (see Sec. 4.1), which can be distinguished in (a). By thresholding the values in (b), the location of the κ-carbides was derived, which is confirmed by the similar dimensions to the κ-carbides detected in the (c) DF image (Fig. 7). (d) The AlNi-rich B2-phase can be distinguished by the correspondingly combined element map. (e) Subsequent thresholding revealed the location of the B2-phase in the maps. In (f), both the κ- and B2-phase are marked in the HAADF image, where the B2-phase was found close to the κ-carbides. *Note: In (b, e), clusters containing fewer than 15 pixels after thresholding were discarded due to a high probability of originating from noise.*

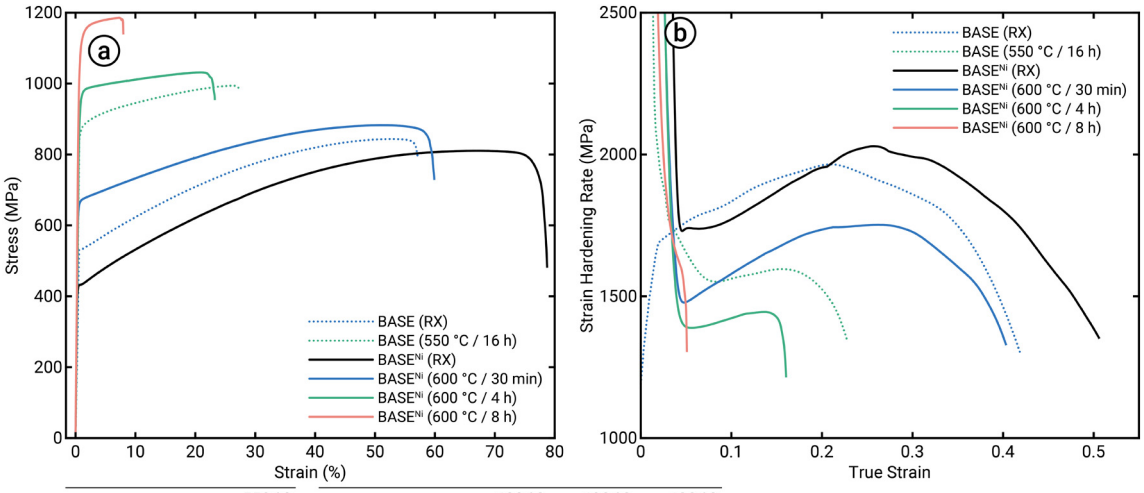

BASE	RX	550 °C 16 h
$R_{p0.2}$ (MPa)	540	880
R_m (MPa)	840	995
A_g (%)	56	26

BASE^{Ni}	RX	600 °C 30 min	600 °C 4 h	600 °C 8 h
$R_{p0.2}$ (MPa)	428	659	934	1067
R_m (MPa)	811	883	1032	1186
A_g (%)	66.3	50.4	20.3	6.7

Fig. 14. Comparison of the (a) engineering stress-strain curves and (b) strain hardening rate-true stress curves between the BASE^{Ni} and BASE [34] alloys in the recrystallized (RX) and annealed states. Higher strengths combined with similar elongation were obtained in BASE^{Ni} compared to BASE.

correlated with the activation of shear band refinement-induced plasticity (SRIP) [17,43,45,46,49,56,57]. In these alloys, the medium stacking-fault energy (SFE) between 80 and 120 mJm^{-2} results in deformation accommodated by undissociated dislocation glide [58–61]. Nevertheless, dislocations are confined to planar glide in the fcc matrix, regardless of the κ-precipitation state. Currently, this phenomenon is not fully understood, but closely linked to interactions of dislocations with short- or long-range ordered regions and related glide plane softening [34,35,62,63]. As a consequence, pronounced planar glide of dislocations results in high strain hardening capacity from the formation of slip bands during deformation and related dynamic grain refinement [34,42,56], i.e. the SRIP mechanism. This deformation mechanism was confirmed in BASE^{Ni} (see Fig. 10) and was also observed in C-alloyed MPEAs with high Mn and Al contents [64,65]. After the precipitation of κ-carbides in the 30 min annealed state, increased amounts of κ-phase are sheared during deformation, which decreases the activity for slip band formation [66] and therefore decreased the strain hardening rate. The same strain hardening progression was observed in the BASE alloy, which supports the finding of the predominant κ-carbide formation below 4 h.

Strengthening in the BASE^{Ni} by a finer grain size can be excluded due to a similar grain size to the BASE alloy [34], so can be the effect of grain boundary phase formation, which also occurred in other κ-carbide strengthened steels after long annealing times [17,35,44,45]. In the BASE^{Ni} alloy, the formation of B2-phase started to occur at 600 °C annealing after 4 h (see Sec. 4.2). According to [26,30,54], these B2-particles share incoherent interfaces with the fcc matrix and thus cannot be sheared during deformation, resulting in dispersion hardening. According to [26,54], dislocations bow out at B2/matrix interfaces and bypass the B2-phase particles, leaving behind a dislocation loop that induces back stresses on the following dislocations and results in higher flow stresses, i.e. the Orowan mechanism. Therefore, higher $R_{p0.2}$ of 54 and 187 MPa (or a 6.1 and 21.3 % increase) were obtained compared to the BASE alloy (Fig. 14a) at 4 and 8 h annealing due to 1.0 and 2.3 vol% of B2-phase, averaging to about 68 MPa vol%$^{-1}$. Dispersion strengthening is frequently used in oxide dispersion-strengthened (ODS) alloys [67–69]. The exact amount of strengthening at room temperature obtained by ODS varies depending on particle size, fraction and alloy. For instance, ODS CoCrFeMnNi alloy containing 0.3 wt% with about 10 to 15 nm in size revealed an increased tensile yield strength of 298 MPa [70].

However, the dispersion hardening also affected the activation of SRIP to some extent. The BASE^{Ni} (600 °C/4 h) alloy showed a reduced strain hardening rate compared to the BASE (550 °C/16 h) alloy, which is an indication for decreased slip band activity [66]. The amount of κ-phase was similar in both states [34], and therefore the back stresses induced on the dislocations by the Orowan mechanism on the finely dispersed B2-particles [26,54] impeded slip band formation in BASE^{Ni}. Since the activation of SRIP in the κ- and B2-phases containing alloy was confirmed by microstructure analysis (see Fig. 10), the SRIP effect must have been retained, albeit with reduced activity.

Even though slip band activity was reduced by the B2-phase, an improved mechanical property profile can be achieved by Ni addition to the BASE alloy, especially with respect to the alloy's strength. With a comparable total elongation in the BASE (550 °C/16 h) and BASE^{Ni} (600 °C/4 h) alloys, $R_{p0.2}$ and R_m were increased in BASE^{Ni} by 54 and 37 MPa, respectively. Furthermore, higher fractions of B2-phase in the BASE^{Ni} (600 °C/8 h) alloy lead to $R_{p0.2}$ and R_m of 1067 and 1186 MPa with a reasonable A_g of 6.7%, which is not achievable using the BASE concept. As the desired B2-phase dispersion hardening was achieved as a result of the initial alloy screening, the introduced methodology can be used as a productive tool for MPEA design. Apart from that, the strengthening effect related to grain refinement [22,57] was beyond the scope of the present study (see Fig. 3). Further tailoring of the microstructure by thermo-mechanical treatments will be investigated separately, which will presumably further improve the mechanical properties.

The precipitation of the B2-phase also had a strong influence on the fracture behavior of the tensile samples (see Fig. 11). Short-time annealing up to the BASE^{Ni} (600 °C/4 h) alloy resulted mainly in the formation of κ-carbides and predominantly ductile fracture behavior. At 4 h, small amounts of intergranular fracture were caused by a thin grain boundary phase (see Fig. 7a). At 8 h, however, intergranular fracture was observed due to much coarser precipitations at grain boundaries (see Fig. 12). According to the composition of the different phases, the formation of fcc and κ-carbides was identified [46,48]. The morphology of the grain boundary phase resembled that of overaged κ-strengthened HMnS [17,44,45], which additionally contained small amounts of the B2-

phase and led to intergranular fracture. In the BASE^{Ni} (600 °C/16 h) alloy, high amounts of 6.8 vol% B2-phase in the fcc matrix (see Fig. 6c) caused embrittlement and premature intragranular fracture.

5. Conclusion

A custom CALPHAD database of the Al-C-Co-Fe-Mn-Ni system was developed and applied for theoretical, thermodynamics-based screening of Ni- and Co-added $Al_{14.6}C_{4.9}Fe_{53.6}Mn_{26.9}$ (at%) alloys. Based on the thermodynamic calculations, novel precipitation strengthened Al-C-Fe-Mn-Ni/Co MPEAs were designed. The alloys were derived from highly alloyed steel concepts and revealed the κ- and B2-phase strengthened $Al_{14.7}C_{4.7}Fe_{49.9}Mn_{26.4}Ni_{4.2}$ as the most promising MPEA of this study. The addition of Ni was found to be efficient for promoting the precipitation of B2-particles, whereas the Co-added alloy revealed no strength improvement from the B2-phase. Detailed microstructural and mechanical characterization was carried out to reveal the underlying mechanisms active during annealing and deformation in the newly developed alloys. The following conclusions can be drawn:

- A preliminary CALPHAD-database for thermodynamics-based phase-stability calculations in the Co-Cr-Fe-Mn-Ni system with incomplete extensions to Al and C was developed. The database was successfully applied for the identification of κ- and B2-phase strengthened fcc-based MPEAs, both for its chemical compositions and related heat treatments.
- Annealing of $Al_{14.7}C_{4.7}Fe_{49.9}Mn_{26.4}Ni_{4.2}$ at 600 °C for <4 h resulted in the formation of spinodally decomposed κ-carbides with a size of ~10 nm, similar to the related steel concept. After prolonged annealing for ≥4 h, AlNi B2-precipitates formed on the numerously available coherent fcc/κ-carbide interfaces, resulting in finely dispersed nanoscale (<5 nm) B2-particles. Concurrently, the fraction of the κ-phase decreased with increasing B2-phase fraction due to a partial dissolution of Al from adjacent κ-carbides.
- During plastic deformation, the slip band refinement-induced plasticity (SRIP) effect enabled pronounced strain hardening in the investigated MPEAs. The introduction of non-shearable B2-precipitates lowered the slip band activity, resulting in a smaller contribution of SRIP to the accommodation of plastic deformation.
- In the $Al_{14.7}C_{4.7}Fe_{49.9}Mn_{26.4}Ni_{4.2}$ alloy, the careful balance of precipitation hardening by the κ-phase (≥ 18.4 vol%), dispersion hardening by the B2-phase (≤2.3 vol%), and the SRIP effect ultimately improved the mechanical performance compared to the initial steel concept, resulting in an optimized strength-ductility combination. An up to 21.3 % yield strength increase was achieved to 1 to 1.2 GPa combined with a total elongation of 20 to 10 %.
- Overaging of $Al_{14.7}C_{4.7}Fe_{49.9}Mn_{26.4}Ni_{4.2}$ resulted in the formation of a grain boundary κ-phase, which caused reduced ductility due to intergranular fracture for moderate annealing times (8 h). While the B2-precipitates caused a high strengthening effect, high fractions of 6.3 vol% inside the matrix after extended annealing (16 h) led to brittle intragranular and premature fracture.

Supplementary data to this article can be found online at https://doi.org/10.1016/j.matdes.2020.109315.

Data availability

The raw/processed data required to reproduce these findings cannot be shared at this time as the data also forms part of an ongoing study.

Declaration of Competing Interest

The authors confirm that there are no known conflicts of interest associated with this publication and there has been no significant financial support beside the stated ones for this work that could have influenced its outcome.

Acknowledgments

The authors would like to thank the Deutsche Forschungsgemeinschaft (DFG, German Research Foundation) for the support of the depicted research within the priority programme 2006 "CCA – HEA" (project-IDs 388166069 and 388544551). B.H. and C.H. also gratefully acknowledge the funding of the DFG under Germany's Excellence Strategy - EXC-2023 Internet of Production - 390621612 and under the Sonderforschungsbereich (SFB, Collaborative Research Center) 761 "Steel - Ab Initio. Quantum Mechanics Guided Design of New Fe-based Materials" (29898171). The help of Yan Ma and Wenwen Song with SYXRD measurements is also gratefully acknowledged.

References

[1] B.S. Murty, J.W. Yeh, S. Ranganathan, P. Bhattacharjee, Chapter 1 - a brief history of alloys and the birth of high-entropy alloys, in: B. Murty, J. Yeh, S. Ranganathan, P. Bhattacharjee (Eds.), High-Entropy Alloys, 2 ed.Butterworth-Heinemann, Boston 2014, pp. 1–12, https://doi.org/10.1016/B978-0-12-816067-1.00001-1.
[2] X. Lim, Mixed-up metals make for stronger, tougher, stretchier alloys, Nature 533 (2016) 306–307, https://doi.org/10.1038/533306a.
[3] J.W. Yeh, S.K. Chen, S.J. Lin, J.Y. Gan, T.S. Chin, T.T. Shun, C.H. Tsau, S.Y. Chang, Nanostructured high-entropy alloys with multiple principal elements: Novel alloy design concepts and outcomes, Advanced Engineering Materials 6 (2004)https://doi.org/10.1002/adem.200300567 299–303+274.
[4] B. Cantor, I.T. Chang, P. Knight, A.J. Vincent, Microstructural development in equiatomic multicomponent alloys, Mater. Sci. Eng. A 375-377 (2004) 213–218, https://doi.org/10.1016/j.msea.2003.10.257.
[5] M.H. Tsai, J.W. Yeh, High-entropy alloys: a critical review, Materials Research Letters 2 (2014) 107–123, https://doi.org/10.1080/21663831.2014.912690.
[6] K.G. Pradeep, C.C. Tasan, M.J. Yao, Y. Deng, H. Springer, D. Raabe, Non-equiatomic high entropy alloys: approach towards rapid alloy screening and property-oriented design, Mater. Sci. Eng. A 648 (2015) 183–192, https://doi.org/10.1016/j.msea.2015.09.010.
[7] D.B. Miracle, J.D. Miller, O.N. Senkov, C. Woodward, M.D. Uchic, J. Tiley, Exploration and development of high entropy alloys for structural applications, Entropy 16 (2014) 494–525, https://doi.org/10.3390/e16010494.
[8] O.N. Senkov, J.D. Miller, D.B. Miracle, C. Woodward, Accelerated exploration of multi-principal element alloys for structural applications, Calphad: Computer Coupling of Phase Diagrams and Thermochemistry 50 (2015) 32–48, https://doi.org/10.1016/j.calphad.2015.04.009.
[9] Y. Ikeda, B. Grabowski, F. Körmann, Ab initio phase stabilities and mechanical properties of multicomponent alloys: a comprehensive review for high entropy alloys and compositionally complex alloys, Mater. Charact. 147 (2019) 464–511, https://doi.org/10.1016/j.matchar.2018.06.019.
[10] Y. Ikeda, I. Tanaka, J. Neugebauer, F. Körmann, Impact of interstitial C on phase stability and stacking-fault energy of the CrMnFeCoNi high-entropy alloy, Physical Review Materials 3 (2019) 113603, https://doi.org/10.1103/PhysRevMaterials.3.113603.
[11] F. Kies, Y. Ikeda, S. Ewald, J.H. Schleifenbaum, B. Hallstedt, F. Körmann, C. Haase, Combined Al and C alloying enables mechanism-oriented design of multi-principal element alloys: Ab initio calculations and experiments, Scr. Mater. 178 (2020) 366–371, https://doi.org/10.1016/j.scriptamat.2019.12.004.
[12] Z. Li, F. Körmann, B. Grabowski, J. Neugebauer, D. Raabe, Ab initio assisted design of quinary dual-phase high-entropy alloys with transformation-induced plasticity, Acta Mater. 136 (2017) 262–270, https://doi.org/10.1016/j.actamat.2017.07.023.
[13] A. Kauffmann, M. Stüber, H. Leiste, S. Ulrich, S. Schlabach, D.V. Szabó, S. Seils, B. Gorr, H. Chen, H.J. Seifert, M. Heilmaier, Combinatorial exploration of the high entropy alloy system co-Cr-Fe-Mn-Ni, Surf. Coat. Technol. 325 (2017) 174–180, https://doi.org/10.1016/j.surfcoat.2017.06.041.
[14] S. Ewald, F. Kies, S. Hermsen, M. Voshage, C. Haase, J.H. Schleifenbaum, Rapid alloy development of extremely high-alloyed metals using powder blends in laser powder bed fusion, Materials 12 (2019) 1706, https://doi.org/10.3390/ma12101706.
[15] E. George, W. Curtin, C. Tasan, High entropy alloys: a focused review of mechanical properties and deformation mechanisms, Acta Mater. 188 (2020) 435–474, https://doi.org/10.1016/j.actamat.2019.12.015.
[16] D.B. Miracle, O.N. Senkov, A critical review of high entropy alloys and related concepts, Acta Mater. 122 (2017) 448–511, https://doi.org/10.1016/j.actamat.2016.08.081.
[17] O.A. Zambrano, A general perspective of Fe–Mn–Al–C steels, J. Mater. Sci. 53 (2018) 14003–14062, https://doi.org/10.1007/s10853-018-2551-6.
[18] O. Kwon, K.Y. Lee, G.S. Kim, K.G. Chin, New trends in advanced high strength steel developments for automotive application, Mater. Sci. Forum 638-642 (2010) 136–141, https://doi.org/10.4028/www.scientific.net/msf.638-642.136.
[19] S. Chen, R. Rana, A. Haldar, R.K. Ray, Current state of Fe-Mn-Al-C low density steels, Prog. Mater. Sci. 89 (2017) 345–391, https://doi.org/10.1016/j.pmatsci.2017.05.002.
[20] J.D. Yoo, K.T. Park, Microband-induced plasticity in a high Mn-Al-C light steel, Mater. Sci. Eng. A 496 (2008) 417–424, https://doi.org/10.1016/j.msea.2008.05.042.
[21] I. Zuazo, B. Hallstedt, B. Lindahl, M. Selleby, M. Soler, A. Etienne, A. Perlade, D. Hasenpouth, V. Massardier-Jourdan, S. Cazottes, X. Kleber, Low-density steels:

complex metallurgy for automotive applications, Jom 66 (2014) 1747–1758, https://doi.org/10.1007/s11837-014-1084-y.
[22] F. Brasche, C. Haase, M. Lipińska-Chwałek, J. Mayer, D.A. Molodov, Combined κ-carbide precipitation and recovery enables ultra-high strength and ductility in light-weight steels, Mater. Sci. Eng. A 795 (2020) 139928, https://doi.org/10.1016/j.msea.2020.139928.
[23] J.Y. He, W.H. Liu, H. Wang, Y. Wu, X.J. Liu, T.G. Nieh, Z.P. Lu, Effects of Al addition on structural evolution and tensile properties of the FeCoNiCrMn high-entropy alloy system, Acta Mater. 62 (2014) 105–113, https://doi.org/10.1016/j.actamat.2013.09.037.
[24] T. Yang, S. Xia, S.S.S.S. Liu, C. Wang, S.S.S.S. Liu, Y. Zhang, J. Xue, S. Yan, Y. Wang, Effects of AL addition on microstructure and mechanical properties of AlxCoCrFeNi high-entropy alloy, Mater. Sci. Eng. A 648 (2015) 15–22, https://doi.org/10.1016/j.msea.2015.09.034.
[25] J.M. Park, J. Moon, J.W. Bae, J. Jung, S. Lee, H.S. Kim, Effect of annealing heat treatment on microstructural evolution and tensile behavior of Al0.5CoCrFeMnNi high-entropy alloy, Mater. Sci. Eng. A 728 (2018) 251–258, https://doi.org/10.1016/j.msea.2018.05.041.
[26] S.-H.H. Kim, H. Kim, N.J. Kim, Brittle intermetallic compound makes ultrastrong low-density steel with large ductility, Nature 518 (2015) 77–79, https://doi.org/10.1038/nature14144.
[27] M. Yang, F. Yuan, Q. Xie, Y. Wang, E. Ma, X. Wu, Strain hardening in Fe–16Mn–10Al–0.86C–5Ni high specific strength steel, Acta Mater. 109 (2016) 213–222, https://doi.org/10.1016/j.actamat.2016.02.044.
[28] A. Rahnama, H. Kotadia, S. Sridhar, Effect of Ni alloying on the microstructural evolution and mechanical properties of two duplex light-weight steels during different annealing temperatures: experiment and phase-field simulation, Acta Mater. 132 (2017) 627–643, https://doi.org/10.1016/j.actamat.2017.03.043.
[29] W. Wang, H. Zhang, M. Yang, P. Jiang, F. Yuan, X. Wu, Shock and spall behaviors of a high specific strength steel: effects of impact stress and microstructure, J. Appl. Phys. 121 (2017) 135901, https://doi.org/10.1063/1.4979346.
[30] A. Rahnama, H. Kotadia, S. Clark, V. Janik, S. Sridhar, Nano-mechanical properties of Fe-Mn-Al-C lightweight steels, Sci. Rep. 8 (2018) 1–12, https://doi.org/10.1038/s41598-018-27345-w.
[31] H. Kim, Strain hardening of novel high Al low-density steel consisting of austenite matrix and B2-ordered intermetallic second phase in the perspective of non-cell forming face-centered-cubic alloy with high stacking fault energy, Scr. Mater. 160 (2019) 29–32, https://doi.org/10.1016/j.scriptamat.2018.09.044.
[32] J. Hwang, T. Trang, O. Lee, G. Park, A. Zargaran, N.J. Kim, Improvement of strength – ductility balance of B2-strengthened lightweight steel, Acta Mater. 191 (2020) 1–12, https://doi.org/10.1016/j.actamat.2020.03.022.
[33] C. Haase, F. Tang, M.B. Wilms, A. Weisheit, B. Hallstedt, Combining thermodynamic modeling and 3D printing of elemental powder blends for high-throughput investigation of high-entropy alloys – towards rapid alloy screening and design, Mater. Sci. Eng. A 688 (2017) 180–189, https://doi.org/10.1016/j.msea.2017.01.099.
[34] C. Haase, C. Zehnder, T. Ingendahl, A. Bikar, F. Tang, B. Hallstedt, W. Hu, W. Bleck, D.A. Molodov, On the deformation behavior of κ-carbide-free and κ-carbide-containing high-Mn light-weight steel, Acta Mater. 122 (2017) 332–343, https://doi.org/10.1016/j.actamat.2016.10.006.
[35] W. Song, W. Zhang, J. Von Appen, R. Dronskowski, W. Bleck, κ-phase formation in Fe-Mn-Al-C austenitic steels, Steel Research International 86 (2015) 1161–1169, https://doi.org/10.1002/srin.201400587.
[36] F. Bachmann, R. Hielscher, H. Schaeben, Grain detection from 2d and 3d EBSD data-specification of the MTEX algorithm, Ultramicroscopy 111 (2011) 1720–1733, https://doi.org/10.1016/j.ultramic.2011.08.002.
[37] G. Nolze, R. Hielscher, Orientations – perfectly colored, J. Appl. Crystallogr. 49 (2016) 1786–1802, https://doi.org/10.1107/s1600576716012942.
[38] A.P. Hammersley, FIT2D: An Introduction and Overview, ESRF Internal Report ESRF97HA02, 1997.
[39] A.P. Hammersley, S.O. Svensson, M. Hanfland, A.N. Fitch, D. Hausermann, Two-dimensional detector software: from real detector to idealised image or two-theta scan, High Pressure Res. 14 (2007) 235–248, https://doi.org/10.1080/08957959608201408.
[40] M. Ferrari, L. Lutterotti, Method for the simultaneous determination of anisotropic residual stresses and texture by x-ray diffraction, J. Appl. Phys. 76 (1994) 7246–7255, https://doi.org/10.1063/1.358006.
[41] X.F. Gu, T. Furuhara, W.Z. Zhang, PTCLab: free and open-source software for calculating phase transformation crystallography, J. Appl. Crystallogr. 49 (2016) 1099–1106, https://doi.org/10.1107/S1600576716006075.
[42] J.J. Xing, Y. Wei, L. Hou, An overview of the effects of alloying elements on the properties of lightweight Fe-(15–35) Mn-(5–12) Al-(0.3–1.2) C steel, Jom 70 (2018) 929–937, https://doi.org/10.1007/s11837-018-2837-9.
[43] M.J. Yao, E. Welsch, D. Ponge, S.M. Haghighat, S. Sandlöbes, P. Choi, M. Herbig, I. Bleskov, T. Hickel, M. Lipinska-Chwalek, P. Shanthraj, C. Scheu, S. Zaefferer, B. Gault, D. Raabe, Strengthening and strain hardening mechanisms in a precipitation-hardened high-Mn lightweight steel, Acta Mater. 140 (2017) 258–273, https://doi.org/10.1016/j.actamat.2017.08.049.
[44] Y. Feng, R.R.R. Song, Z. Pei, R.R.R. Song, G. Dou, Effect of aging isothermal time on the microstructure and room-temperature impact toughness of Fe–24.8Mn–7.3Al–1.2C austenitic steel with κ-carbides precipitation, Met. Mater. Int. 24 (2018) 1012–1023, https://doi.org/10.1007/s12540-018-0112-9.
[45] D. Liu, M. Cai, H. Ding, D. Han, Control of inter/intra-granular κ-carbides and its influence on overall mechanical properties of a Fe-11Mn-10Al-1.25C low density steel, Mater. Sci. Eng. A 715 (2018) 25–32, https://doi.org/10.1016/j.msea.2017.12.102.
[46] C.W. Kim, S.I. Kwon, B.H. Lee, J.O. Moon, S.J. Park, J.H. Lee, H.U. Hong, Atomistic study of nano-sized κ-carbide formation and its interaction with dislocations in a cast Si added FeMnAlC lightweight steel, Mater. Sci. Eng. A 673 (2016) 108–113, https://doi.org/10.1016/j.msea.2016.07.029.
[47] W. Lu, R. Qin, Influence of κ-carbide interface structure on the formability of light-weight steels, Mater. Des. 104 (2016) 211–216, https://doi.org/10.1016/j.matdes.2016.05.021.
[48] J. Moon, S.-J. Park, J.H. Jang, T.-H. Lee, C.-H. Lee, H.-U. Hong, D.-W. Suh, S.H. Kim, H.N. Han, B.H. Lee, Atomistic investigations of κ-carbide precipitation in austenitic Fe-Mn-Al-C lightweight steels and the effect of Mo addition, Scr. Mater. 127 (2017) 97–101, https://doi.org/10.1016/j.scriptamat.2016.08.036.
[49] I. Gutierrez-Urrutia, D. Raabe, High strength and ductile low density austenitic FeMnAlC steels: simplex and alloys strengthened by nanoscale ordered carbides, Mater. Sci. Technol. 30 (2014) 1099–1104, https://doi.org/10.1179/1743284714Y.0000000515.
[50] C. Drouven, B. Hallstedt, W. Song, W. Bleck, Experimental observation of κ-phase formation sequences by in-situ synchrotron diffraction, Mater. Lett. 241 (2019) 111–114, https://doi.org/10.1016/j.matlet.2019.01.062.
[51] M.J. Yao, P. Dey, J.B. Seol, P. Choi, M. Herbig, R.K. Marceau, T. Hickel, J. Neugebauer, D. Raabe, Combined atom probe tomography and density functional theory investigation of the Al off-stoichiometry of κ-carbides in an austenitic Fe-Mn-Al-C low density steel, Acta Mater. 106 (2016) 229–238, https://doi.org/10.1016/j.actamat.2016.01.007.
[52] Z.Q. Wu, H. Ding, H.Y. Li, M.L. Huang, F.R. Cao, Microstructural evolution and strain hardening behavior during plastic deformation of Fe-12Mn-8Al-0.8C steel, Mater. Sci. Eng. A 584 (2013) 150–155, https://doi.org/10.1016/j.msea.2013.07.023.
[53] J.C. Rao, V. Ocelík, D. Vainchtein, Z. Tang, P.K. Liaw, J.T.M. De Hosson, The fcc-bcc crystallographic orientation relationship in AlxCoCrFeNi high-entropy alloys, Mater. Lett. 176 (2016) 29–32, https://doi.org/10.1016/j.matlet.2016.04.086.
[54] H. Song, J. Yoo, S.-H. Kim, S.S. Sohn, M. Koo, N.J. Kim, S. Lee, Novel ultra-high-strength cu-containing medium-Mn duplex lightweight steels, Acta Mater. 135 (2017) 215–225, https://doi.org/10.1016/j.actamat.2017.06.035.
[55] S. Jiang, H. Wang, Y. Wu, X. Liu, H. Chen, M. Yao, B. Gault, D. Ponge, D. Raabe, A. Hirata, M. Chen, Y. Wang, Z. Lu, Ultrastrong steel via minimal lattice misfit and high-density nanoprecipitation, Nature 544 (2017) 460–464, https://doi.org/10.1038/nature22032.
[56] E. Welsch, D. Ponge, S.M. Hafez Haghighat, S. Sandlöbes, P. Choi, M. Herbig, S. Zaefferer, D. Raabe, Strain hardening by dynamic slip band refinement in a high-Mn lightweight steel, Acta Mater. 116 (2016) 188–199, https://doi.org/10.1016/j.actamat.2016.06.037.
[57] F. Ji, W. Song, Y. Ma, C. Li, W. Bleck, G. Wang, Recrystallization behavior in a low-density high-Mn high-Al austenitic steel undergone thin strip casting process, Mater. Sci. Eng. A 733 (2018) 87–97, https://doi.org/10.1016/j.msea.2018.07.023.
[58] G. Frommeyer, U. Brüx, Microstructures and mechanical properties of high-strength Fe-Mn-Al-C light-weight TRIPLEX steels, Steel Research International 77 (2006) 627–633, https://doi.org/10.1002/srin.200606440.
[59] J.D. Yoo, S.W. Hwang, K.T. Park, Origin of extended tensile ductility of a Fe-28Mn-10Al-1C steel, Metallurgical and Materials Transactions A: Physical Metallurgy and Materials Science 40 (2009) 1520–1523, https://doi.org/10.1007/s11661-009-9862-9.
[60] H. Ding, D. Han, J. Zhang, Z. Cai, Z. Wu, M. Cai, Tensile deformation behavior analysis of low density Fe-18Mn-10Al-xC steels, Mater. Sci. Eng. A 652 (2016) 69–76, https://doi.org/10.1016/j.msea.2015.11.071.
[61] I. Gutierrez-Urrutia, D. Raabe, Influence of Al content and precipitation state on the mechanical behavior of austenitic high-Mn low-density steels, Scr. Mater. 68 (2013) 343–347, https://doi.org/10.1016/j.scriptamat.2012.08.038.
[62] V. Gerold, H.P. Karnthaler, On the origin of planar slip in f.c.c. alloys, Acta Metall. 37 (1989) 2177–2183, https://doi.org/10.1016/0001-6160(89)90143-0.
[63] S. Sevsek, F. Brasche, C. Haase, W. Bleck, Combined deformation twinning and short-range ordering causes serrated flow in high-manganese steels, Mater. Sci. Eng. A 746 (2019) 434–442, https://doi.org/10.1016/j.msea.2019.01.042.
[64] Z. Wang, I. Baker, W. Guo, J.D. Poplawsky, The effect of carbon on the microstructures, mechanical properties, and deformation mechanisms of thermo-mechanically treated Fe40.4Ni11.3Mn34.8Al7.5Cr6 high entropy alloys, Acta Materialia 126 (2017) 346–360, https://doi.org/10.1016/j.actamat.2016.12.074.
[65] Z. Wang, H. Bei, I. Baker, Microband induced plasticity and the temperature dependence of the mechanical properties of a carbon-doped FeNiMnAlCr high entropy alloy, Mater. Charact. 139 (2018) 373–381, https://doi.org/10.1016/j.matchar.2018.03.017.
[66] K. Choi, C.-H.H. Seo, H. Lee, S.K. Kim, J.H. Kwak, K.G. Chin, K.-T.T. Park, N.J. Kim, Effect of aging on the microstructure and deformation behavior of austenite base light-weight Fe-28Mn-9Al-0.8C steel, Scr. Mater. 63 (2010) 1028–1031, https://doi.org/10.1016/j.scriptamat.2010.07.036.
[67] J.S. Benjamin, M.J. Bomford, Dispersion strengthened aluminum made by mechanical alloying, Metall. Trans. A. 8 (A) (1977) 1302–1305, https://doi.org/10.1007/BF02643845.
[68] R.L. Klueh, J.P. Shingledecker, R.W. Swindeman, D.T. Hoelzer, Oxide dispersion-strengthened steels: a comparison of some commercial and experimental alloys, J. Nucl. Mater. 341 (2005) 103–114, https://doi.org/10.1016/j.jnucmat.2005.01.017.
[69] L. Raman, K. Gothandapani, B.S. Murty, Austenitic oxide dispersion strengthened steels: A review, 2016https://doi.org/10.14429/dsj.66.10205.
[70] H. Hadraba, Z. Chlup, A. Dlouhy, F. Dobes, P. Roupcova, M. Vilemova, J. Matejicek, Oxide dispersion strengthened CoCrFeNiMn high-entropy alloy, Mater. Sci. Eng. A 689 (2017) 252–256, https://doi.org/10.1016/j.msea.2017.02.068.